Advanced Powder Technology 25 (2014) 56–70

Contents lists available at ScienceDirect

Advanced Powder Technology

journal homepage: www.elsevier.com/locate/apt

Invited review paper

New developments in spark production of nanoparticles

T.V. Pfeiffer, J. Feng, A. Schmidt-Ott *

Department of Chemical Engineering, Delft University of Technology, Delft 2628 BL, Netherlands

ARTICLE INFO

Article history:
Received 3 October 2013
Received in revised form 28 November 2013
Accepted 9 December 2013
Available online 22 December 2013

Keywords:
Spark
Nanoparticle
Mixing
Spark energy
Atomic clusters

ABSTRACT

The paper selects a number of recent developments in spark production of nanoparticles that are important for production of nanopowders and nanoparticulate materials. It explains the method, including recent improvements, and refers to theoretical considerations as well as practical experience in controlling the main particle parameters determining the product properties, namely size and composition. The paper focusses on particles below 10 nm, where the spark method works best. Values for feasible production rates and energy efficiencies are estimated using published data. Spark mixing is identified as a feature that renders great potential to the method, especially for catalysis but also for other purposes, as it opens myriads of new possibilities in the form of material combinations. The most important condition for this potential to turn into industrial application is the capability of scaling up. The basic principles that allow mixing are treated, methods are reviewed and examples for applications are given. These include the creation of new phases that only exist in the nanoparticulate state. A new technique allowing an increase of the production rate of a single electrode pair by a factor of 10^2–10^3 is introduced. It allows production nanoparticles typically 5 nm in size at a rate of 1 g/h, and this rate can arbitrarily be increased further by operating multiple sparks in parallel. The energy requirement is in the order of 3 kWh/g. The paper stems on adoption and interpretation of published articles as well as on new developments that are presented for the first time.

Contents

* Corresponding author. Tel.: +31 152783577.
E-mail address: A.Schmidt-Ott@tudelft.nl (A. Schmidt-Ott).

0921-8831/$ - see front matter
http://dx.doi.org/10.1016/j.apt.2013.12.005

1. Introduction

1.1. Objective of this publication

The present paper selects some published and unpublished developments in spark production that are, in our view, of principle importance in view of production of nano-powders and materials based on or containing nanoparticles. Much emphasis is laid on a unique feature of the spark method: the potential of mixing virtually any inorganic substance with any other inorganic substance(s) on a scale of nanometers or smaller. We refer to this feature as spark mixing. We are convinced that it is mainly this feature that renders great potential to the method, both for future industrial and research purposes. Spark mixing will, in our opinion, lead to the discovery and fabrication of completely new materials that cannot be produced effectively by any other method. In particular, this technique is poised to lead to a revolution in the field of heterogeneous catalysis, where the mixing capabilities allow the design of primary catalyst particles of a virtually unlimited number of compositions. We believe it will play an important role in replacing expensive noble metals by less expensive species like mixed transition metal oxides. Apart from homogeneous (atomic) mixtures, the flexible combination of different components mixed on a nanoscale is bound to lead to new possibilities. One prerequisite for practical application is the capability of producing sufficient quantities. The absence of scaled-up production is a major reason for the absence of any breakthrough in this field until now. Another task to be solved is creation of robust, hierarchical structures: porous on a nanoscale and preferably with varying pore dimensions from nano- to micrometers. The whole task is structuring all the way from atomic, via nanometer to micrometer dimensions, called micro- meso- and macrostructure in the field of catalysis. For catalysis, these structures do not need to be regular or follow specific geometrical patterns, as long as automatic ordering on the atomic scale provides the desired catalytically active sites. The random process of spark mixing, including nanoparticle agglomeration in the aerosol phase or in surface deposition, is believed to render an important contribution to this field.

The present paper therefore dedicates much attention to atomic and nanomixing and to unpublished crucial steps in scaling up. Existing approaches of creating porous, high surface area structures are briefly treated as well. The mixing part concentrates on published work, which has mainly been carried out in the group of the authors at Delft University of Technology, without wanting to diminish the value of the contributions of others. New considerations about feasible mass production rates and energy efficiency, based on published data, are presented. To begin with we describe the method in Section 2, and refer to particle size control – a crucial feature, as particle size determines the properties of the product just as the chemical composition does – in Section 3. For further reading on spark preparation of nanoparticles, we refer to a recent review by Meuller et al. [1]. This review from Lund University focuses on existing spark generator construction concepts, considerations concerning the discharge itself and classical particle growth principles. It explains numerous applications.

1.2. Historical sketch of spark production of nanoparticles

The phenomenon of sparks occurring between electrodes and ablating them has been known for a long time, for instance as an undesired effect on spark plugs in gasoline engines. The evaporation per spark has been related to the energy dissipated [2] back in 1950. Continuous discharges were applied for producing particles in gasses in the early 20th century [3], but, to our knowledge, sparks were not applied for the purpose of nanoparticle production until first reported by Burtscher and Schmidt-Ott in 1984 [4]. A detailed description of the method by Schwyn, Garwin and Schmidt-Ott followed in 1988 [5]. This paper already demonstrates that particles as small as 1 nm in size can be produced by the method, and the production of particles ranging in size from the single atom to 100 nm by spark ablation have been reported since then in a large number of publications and PhD theses. The method was commercialized as a source of carbon particles in 1993 [6]. A notable publication about spark production of particles in liquids appeared in 1987 [7]. The review by Meuller et al. [1] and its references are recommended as further sources of literature on the method.

1.3. Features of spark production of nanoparticles

Spark production of nanoparticles is based on ablation of electrodes by inducing spark discharges between them. The particles produced have much in common with those produced by laser ablation [8–10], a method that is well established as a means of producing nanoparticles in quantities not exceeding milligrams for research purposes. The great attention that the spark has drawn as a competing principle primarily stems from the fact that the costs are much lower, because no laser is required. Secondly, nanoparticle production by spark discharge is scalable. The European project "Buonapart-E", started in 2012 and joining 21 European partners, has scaling up of the spark method as an objective. The project was granted mainly on the grounds of the process being environmentally friendly, as no chemical precursors are required and no waste is produced.

In its original form the method applies no chemicals except the substance or mixture of substances that are supposed to compose the particles. Other notable features of the method are the feasibility of very high purity, enabling non-oxide particle production even for magnesium-based materials [11]. The particles are usually crystalline, and their presence in the aerosol phase after production allows reactive modification such as oxidation and size selection. The particles can, if desired, be brought into liquids, e.g. by bubbling [12]. Where purity is not a major concern, sparking in the liquid is also a possibility [7].

2. The method of spark production of nanoparticles

Fig. 2.1 shows the basic topology of a spark generator. Repeated sparks are produced between electrodes, and a gas flow, usually an inert gas, carries the formed particles away from the production volume. Meuller et al. [1] give an overview of the configurations applied to date. Numerous general studies on the phenomenon of spark discharge have been published [13]. A review on atmospheric pressure discharges connected with nanoparticle production has been written by Borra [14], but the knowledge on the complex process from plasma formation to nanoparticle formation is limited. Each spark consists of a plasma between two electrodes (Fig. 2.1(a)) during the time of typically a few microseconds, the temperature of which is around 20,000 K [15]and higher [16]. This

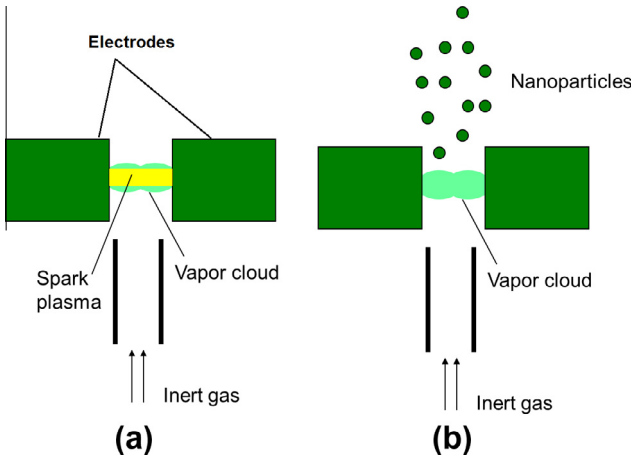

Fig. 2.1. The basic topology of a spark generator.

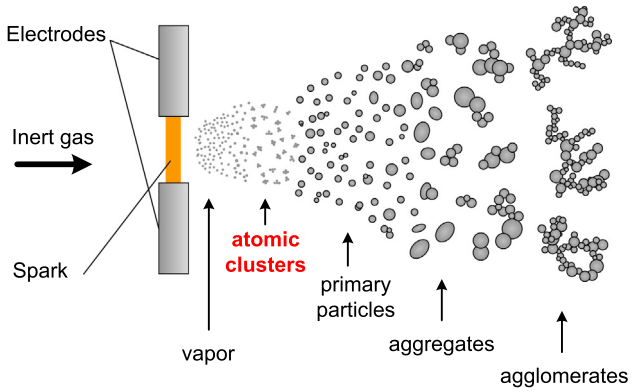

Fig. 2.2. States of particle formation by spark discharge.

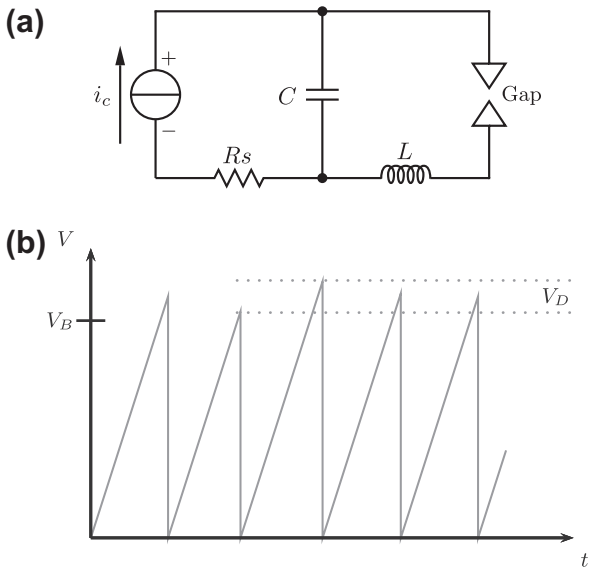

Fig. 2.3. (a) Classical circuit of spark nanoparticle generator and (b) voltage across spark gap vs. time.

leads to rapid heating of small "hot spots" on the electrodes, where the electrode material is "instantaneously" heated to the boiling point. After extinction of the spark, the vapor plume formed in the vicinity of the electrodes by each spark (see Fig. 2.1) is cooled by adiabatic expansion and by mixing with the surrounding flowing gas (Fig. 2.1(b)), and condenses to form particles in the nanometer size regime or smaller. Depending on the composition of the vapor plume, a broad range of material classes, including pure metals, alloys, non-alloyed composites, semiconductors, oxides, hydrides, etc., can be synthesized. Examples of spark generated materials are provided in Table 2.1. Section 6 further illustrates this process in connection with mixing of different materials.

Fig. 2.2 illustrates the formation of atomic clusters, nanoparticles and agglomerates of these from the vapor. By adjusting the concentration of the evaporated material in the initial phase of particle formation, the product can be tuned from atoms to nanoparticulate agglomerates. This "end state" is reached during a feasible time in the continuous flow arrangement. The initial concentration is controlled by the energy per spark and the process gas flow rate through the spark zone, and sometimes also by a further dilution step. Practical ways of influencing the particle size are further discussed in Section 3.

Basically, electrical power has to be transferred to the discharge. The "classical" circuit (Fig. 2.3(a)), introduced in the original papers, is elegant due to its simplicity. Using the spark itself as a switch, it does not require any fast switching electronics. The current source charges the capacitance C, and when its voltage reaches the value for gas breakdown, the spark occurs, discharges the capacitor and the process repeats itself. Drawbacks of this concept are the irregularity in the breakdown voltage V_B, illustrated in the voltage vs. time curve in Fig. 2.3(b) and causing an irregularity in the energy per spark, E_s, according to

$$E_s = 1/2CV_s^2 \quad (1)$$

Another drawback of the simple circuit is that its operation at repetition frequencies higher than 500 Hz is not feasible (see Section 5). Nevertheless, it has been applied almost exclusively in spark ablation literature until now.

Table 2.1
Selection of materials synthesized by spark discharge. References to literature and sections of this paper are included.

Material class	System	Ref.	Section	Notes
Metal	W, Cu, Ag, Nb, Pd, Au, Mg, Sb	[25]		–
	Mg	[11]		Special precautions with regards to O_2 needed
Alloy	Fe/Cu, Fe/Zn	[38]		Two different electrodes
	Cr/Co	[39]		Alloy electrodes
	SnSb, Cu_2Sb	[41]		Sintered electrodes
	Cu–W, Ag–Cu, Pt–Au	[40]	6.2	Non-alloying metals
Semiconductor	Si	[19]	2	Doped electrodes
	Ge	[56]		–
Oxide	CdO, Fe_2O_3	[49]	6.4	3% O_2 in Ar
	MgO	[11]		99.999% Ar
Carbon composite	Ag/C	[57]		Metal & graphite rods. Various morphologies
	Cu/C	[58]		2 ppm C_2H_2 in Ar. Amorphous carbon shell
Particulate composite	Mg with Pd or Nb catalyst	[11,42]	6.3	2 Sparks in series

These drawbacks can be circumvented by applying a switched pulse generator (Fig. 2.4), providing short pulses of sufficient voltage and current. One such example is the "spark plug" circuit [17], which has hardly been applied for nanoparticle production due to practical limitations in the energy per spark. In order to avoid having to ignite the spark every time, a continuous current supply can keep a low-power discharge going, not causing any evaporation. The pulsing network then superimposes current peaks delivering the desired short sparks [18]. This concept has very recently been developed and is firstly described in Section 5 in connection with scaling up.

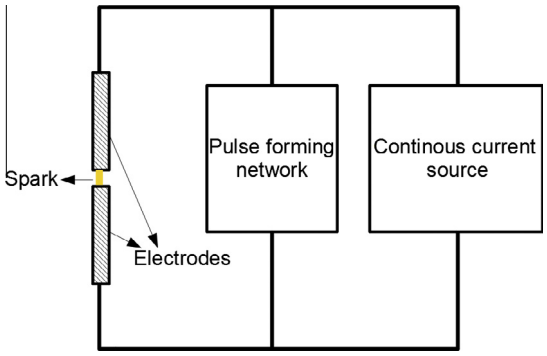

Fig. 2.4. "General" spark circuit, containing pulse forming network and continuous current supply.

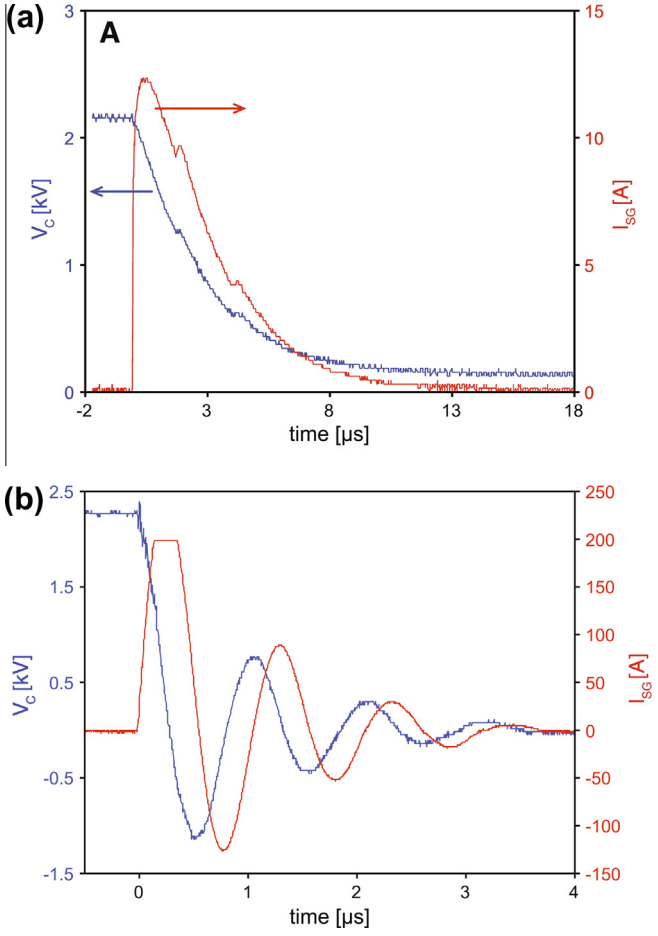

Fig. 2.5. Oscilloscope traces for a typical spark event (red curve: current, blue curve: voltage) (a) for intrinsic Si electrodes (overcritical Damping); (b) for boron-doped Si (undercritical damping).

Fig. 2.5 shows the current and voltage vs. time for the moment of discharge for undoped Si and doped Si [19]. In the second case, the voltage and current perform an under-damped oscillation, as is usually seen with the classical circuit. This is due to the inductance of the wires forming the circuit (see Fig. 2.5(b)), which leads to the typical behavior of an RLC circuit. In the first case, the large resistance of the Si electrodes causes overcritical damping, and no voltage reversal is seen. This damping is accompanied by dissipation of a large part of the energy, and this limits the feasibility of spark ablation to semiconductors. In order to obtain good results, the electrode resistance should be decreased, e.g. by doping. As the negative electrode is ablated more strongly than the positive one due to positive ion bombardment, this voltage reversal is desired in many cases, as the electrodes are ablated more equally. It also has relevance for spark mixing, as shown in Section 6.

3. Particle size control

3.1. Effects controlling the particle diameter

The primary particle diameter distribution of spark produced, is usually near-lognormal, with relative standard deviations around the self-preserving value of 1.46 and below this value for particles smaller than 3 nm. The geometric means or peak values are generally smaller than 10 nm. Apart from the chemical and crystalline composition, it is the primary particle size that defines properties of the material produced. According to Koch and Friedlander [20], the primary particle size is the diameter for which the collision time equals the coalescence time at the temperature the aggregates form. In spark ablation, the particles the agglomerates consist of are usually quite round, as illustrated in Fig. 2.2, which means that sintering leads to complete coalescence at the aggregation stage. The primary particle diameter can be defined as the size of the largest coalesced units.

Usually, soft agglomerates are formed, consisting of primary particles held together by van der Waals forces. This is ascribed to the fact that most of the agglomeration takes place at room temperature, where usually no sintering occurs. Agglomerate reconstruction experiments are a tool to determine interparticulate forces [21] and have confirmed this statement. Agglomerate reconstruction in the aerosol phase is induced by gradual increase of the aerosol temperature and subsequent measurement of the size distribution [21,22], or by a liquid condensing on the particles close to room temperature [23].

It is to be noted that transmission electron micrographs often show necks between primary particles, which tend to form under the influence of the electron beam. Some heating is inevitable in TEM, and this very easily leads to sintering, especially between metal primary particles smaller than 5 nm, but this was also seen with Si, see Fig. 3.1 [19]. Where un-sintered primary particles form the agglomerate, this is often due to a thin surface film of a physisorbed or chemisorbed species, forming a sintering barrier. The electron beam may instantaneously remove this barrier, and sintering occurs. This artifact makes it difficult or impossible to determine the "true" primary particle diameter. Furthermore, the primary particle size is hard to reproduce, because of impurities that hinder coalescence. For this reason, the coalescence time in the Koch–Friedlander criterion must be extremely sensitive to any kind of surface contamination and thus depends on very small traces of adsorbed gas constituents or impurity atoms segregating to the nanoparticle surface.

The above-mentioned difficulties of reproducible experiments and reliable primary particle size determination are not present,

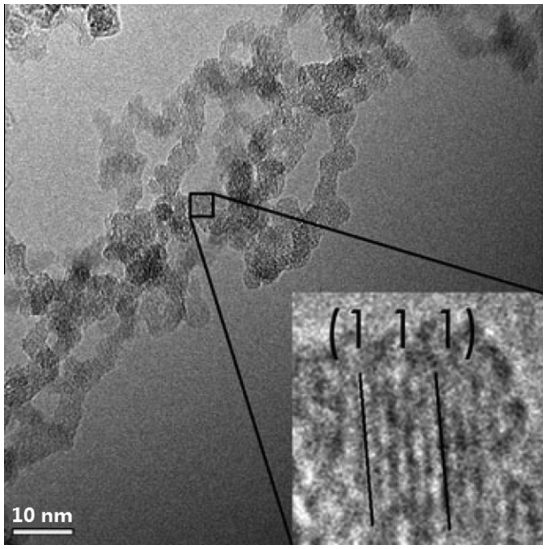

Fig. 3.1. TEM micrographs of Si particles produced from boron-doped electrodes. Insert shows a 3.18 Å lattice spacing identified as the (1 1 1) plane of Si [19].

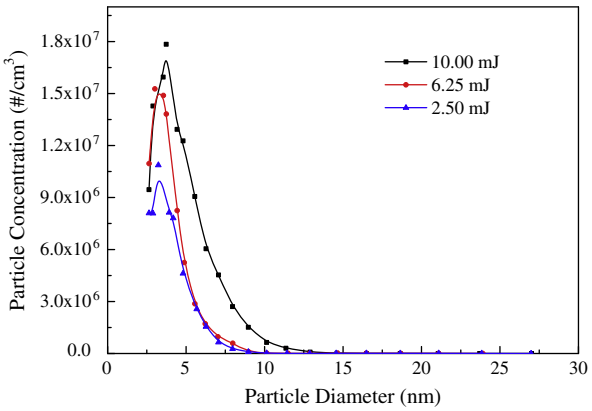

Fig. 3.3. Influence of spark energy on the particle size distribution in the primary particle regime (d = 1 mm, f = 10 Hz, Q = 10 L/min, Ar) (reproduced from Tabrizi et al. [25]).

if the process ends at the state of primary particle growth (Fig. 2.2), i.e. where the coalescence time is shorter than the collision time, and complete coalescence occurs at every collision. Under very clean conditions, gold particles even sinter at room temperature until they reach a size of around 5 nm. This has to do with the fact that metal nanoparticles, if small enough, have a liquid-like surface layer [24], which promotes coalescence. Fig. 3.2 shows the mean mobility particle size as a function of the flow rate [25] for gold particles. Feng et al. (publication in preparation) reveal agglomeration below a certain flow rateand un-agglomerated, round particles above that. In the high flow region, dilution stops the growth process at the stage of primary particle formation (see Fig. 2.2). Further experiments within this flow regime show that the energy per spark determines the (primary) particle size, as seen in Fig. 3.3 [25]. This is easy to understand, qualitatively, as the spark energy directly controls the initial vapor quantity (see Section 5), which influences the initial concentration. The flow rate usually does not have too much influence on this initial concentration, as, in the applied configuration, most of the flow does not go through the initial particle formation zone, which is between the electrodes and in their close vicinity. The influence of the flow rate on the primary particle size can be increased, by blowing a confined flow directly to the spark region. This was already done by Schwyn et al. [5] and led to formation of 1 nm particles. We reconstructed from comparison with our more recent experiments that the spark energy they used must have been about 23 mJ per spark.

As in laser ablation, spark ablation occasionally forms round particles, much larger than the majority of the primary particles. An example is shown in Fig. 3.4 [25]. The mass portion represented by these is usually small, but they may have to be considered as disturbing in applications. The origin of these particles can probably be seen in connection with the process of explosive evaporation, see Section 6, or by acoustic ejection of a droplet from a liquid pool [26]. It is plausible that the droplets rapidly solidify. The conditions under which such particles form and under which they do not form have not been identified yet in systematic studies. From our experience we believe that there is a higher tendency of their formation with a growing energy per spark. Reducing the spark duration with constant energy per spark probably does not eliminate the problem, as simulations done for very short durations (nanoseconds and shorter) in laser ablation still reveal these liquid ejections [27,28]. If several consecutive sparks hit the same spot, this may cause local electrode heating, which may increase the tendency of acoustic droplet ejection. We intend to study this phenomenon and possible solutions in connection with the scaling up of the spark generator.

Often, round, crystalline particles, larger that the obtainable primary particle sizes are desired. In principle, the coalescence size can be increased for this purpose by heating during the agglomeration phase of Fig. 2.2. In terms of the Koch–Friedlander model [20], this has the effect of decreasing the coalescence time, so that it meets the collision time at a later stage. Unagglomerated round

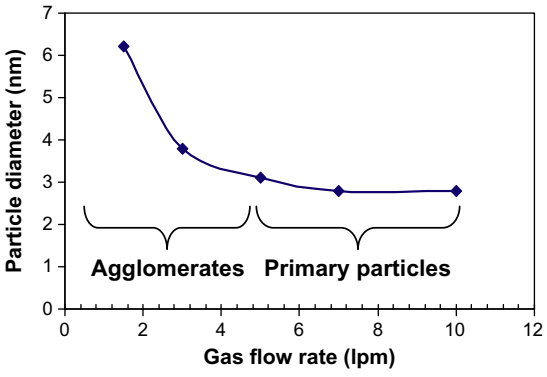

Fig. 3.2. Particle mean diameter as function of Ar mass flow rate (C = 5 nF, d = 0.5 mm, f = 10 Hz).

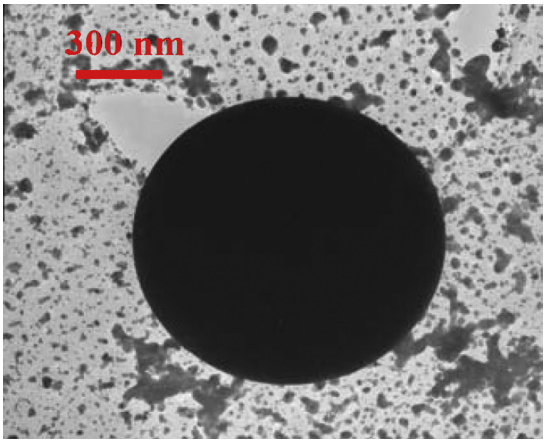

Fig. 3.4. TEM image of large particle Au [25].

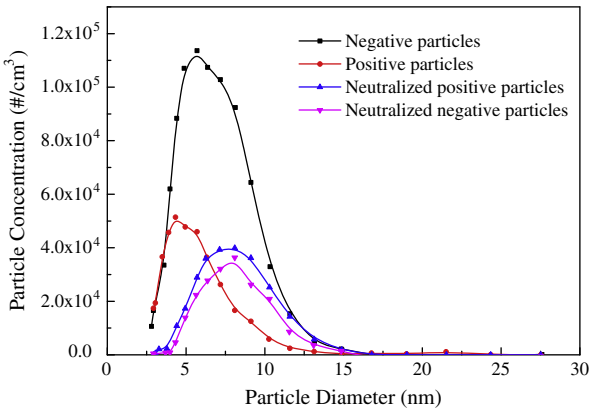

Fig. 3.5. Concentration of charged particles exiting the DMA for Ag compared to "Neutralized", referring to conventional bipolar charging [25].

particles are also obtainable by leading the spark aerosol through a heated tube at its "end stage" [29]. At the appropriate temperature, the agglomerates are melted to form spherical, crystalline particles. Caution should be taken in cases where extreme purity is required. Most heated tube materials release traces that adsorb to the particle surface and may alter their properties.

3.2. Mobility size classification of spark aerosols

If particles of a particular size are required, a narrow size interval of spark-produced particles can be selected by mobility classification in so-called Differential Mobility Analyzers (DMAs). This method is routinely applied [1] for applications where small amounts of material are needed. In the group of Kruis, a scaled-up version of the SMPS principle [30] has been constructed to broaden the range of applications, and this fits together well with scaling efforts concerning the spark generator (see Section 5).

Particle charging is essential for this method to work, and little has been written on the charging probability of very small spark-produced particles. A so-called bipolar charger [31] is customarily applied to obtain a well-defined charging probability of the particles for quantitative determination of the size distribution from the mobility distribution. In Fig. 3.5, the size distribution of charged particles from the spark is compared to the size distribution for the same particles that have undergone bipolar charging [25]. For 4 nm particles the negative charging probability the particles obtained from the spark is more than an order of magnitude higher than in bipolar charging, and this ratio grows further with decreasing particle size. The larger portion of negative particles is attributed to selective loss of positive particles due to the electric field situation in the spark chamber. An asymmetry in the other direction occurs under very clean conditions and has been reported by Vons et al. [11]. Under the absence of electronegative species, electrons do not form negative ions, and due to their very high mobility they are lost in the electric field. The relatively high charging probability for very small particles can be explained with an increased temperature in the zone where the particles are exposed to electrons and positive ions in the vicinity of the spark. This effect makes spark ablation a useful technique for producing charged particles down to the size range of atomic clusters and even single atoms in inert gas suspension and size-classifying them with a DMA. The spark has already been applied in atomic cluster research [32]. We believe that the combination with aerosol technology will lead to new perspectives in this field. In particular, it will become possible to produce atomic clusters in much larger quantities than this has been possible with conventional vacuum-based methods. Studies in this direction are already running in Delft.

3.3. Summary of size control

Summarizing, the agglomerate diameter, measured in many studies on spark formation of nanoparticles, is not the relevant measure when it comes to material properties. Instead we must look at the primary particle size, which is hard to determine. Agglomerate reconstruction measurements can be helpful here. The primary particle diameter can effectively be controlled via the energy per spark and through turbulent dilution by confining the gas stream near the spark, which will be described in detail in a publication in preparation by Feng et al. Size control can be aided by combination of the spark with mobility size classification in a DMA. As charging represents a major obstacle in applying this method to particles a few nanometers or less in diameter, the relatively high charged portion of nanoparticles emerging from the spark is a great advantage. To extend the range of particle sizes the spark can produce from 10 nm upwards, heat-induced coalescence can be used.

4. Energy efficiency and mass production rate

A simple model describing the mass loss of electrodes due to spark ablation has been proposed back to 1950 by Llewellyn Jones [2]. It uses the implicit assumption that a constant portion of the energy dissipated in the spark is transferred to the electrodes for evaporation of material. This means that heating of the gas by the plasma and radiation from the spark itself into the empty volume are not considered in the model, but only the energy transferred to the electrodes. From there it is partly lost to the process by heat conduction and radiation. The electrode temperature at the hot spot never goes beyond the boiling point. These assumptions lead to the following energy balance:

$$\alpha E_s - \pi r^2 \sigma \tau T_b^4 - 2\pi r \tau k (T_b - T) = m c_{ps}(T_m - T) + m c_{pl}(T_b - T_m) + m H_m + m H_v \quad (2)$$

The material mass is m, and c_{ps} and c_{pl} are the heat capacities of the solid and liquid material, respectively. τ is the spark duration and r is the radius of the spark or the radius of the circular heated spot, where the spark impinges on the electrode. The first term on the left represents the portion α of the spark energy E_s, which heats the electrodes. The following terms stand for the heat loss of the heated spot by radiation and by thermal conduction, respectively. The thermal conductivity of the electrode material is denoted by k, and the electrode temperature far from the heated spot is assumed to be room temperature, T. The right hand side expresses the energy required for bringing the material from room temperature, T, to the vapor phase. The first term represents the energy for heating from T to the melting point T_m, the second term is the corresponding energy from T_m to the boiling point, T_b. The following two terms are the enthalpies of melting and evaporation given by H_m and H_v, respectively.

Fig. 4.1 shows the result of a fit of this mass balance to experimental values for the electrode mass loss for several metals. As r and τ are not precisely known, they are used as fitting parameters as well as α. For σ the Stefan Boltzmann constant is used, assuming a black body. The best fit is achieved with $r = 1.5$ µm and $\tau = 1.2$ µs, which are reasonable values. The model predicts the general trend rather well. The deviations can be understood from two phenomena not considered in the model: ejection of liquid material by 'splashing' [26], and chemical reactions such as oxidation. Splashed droplets either impinge and stick on the opposing electrode – resulting in a drop in the measured evaporation rate as seen for Cu –, or escape from the gap – leading to an increase in observed evaporation rate as seen for Au. The situation is more complex if oxidation is considered, as the physical proper-

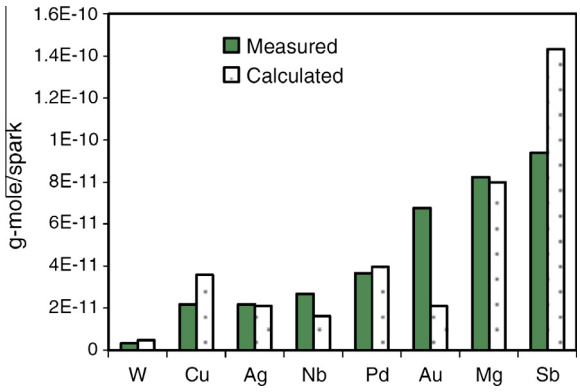

Fig. 4.1. Electrode material loss for various electrodes ($C = 20$ nF, $d = 1$ mm, $f = 100$ Hz, $Q = 0.8$ L/min, Ar) [25].

ties of various oxides, including the reduced conductivity of the electrode, must be taken into account. Finally, the model does not account for the possibility of superheating the electrode material, as explained in Section 6.

As the heat capacities of the liquid and the solid, c_{pl} and c_{ps}, are similar, the result is insensitive to the boiling temperature, T_b. The radiation term is usually small with respect to heat conduction to the electrodes. Fig. 4.2, where the ablated mass is plotted vs. the spark energy (Au in Ar), is consistent with proportionality between the ablated mass with the energy per spark, E_s. This result suggests that for most spark energies applied, heat conduction loss is of small significance. For a given energy, the spark duration must be short enough to meet this condition, so that $\frac{\alpha E_s}{\tau} \gg 2\pi rk$. The energy requirement per unit of particulate mass is then a material dependent constant that can be written as

$$E' = \frac{E_s}{m} = \frac{1}{\alpha}(H_m + H_v + c_{ps}(T_m - T) + c_{pl}(T_b - T_m)) \quad (3)$$

Together with Fig. 4.2, we get $\alpha = 1.5456 \times 10^{-3}$ as an experimental value. That means only about 0.15% of the spark energy is consumed for particle production. Note that this value of α has been derived for an electrode distance of 1 mm and an electrode diameter of 6 mm. It is to be assumed that α is quite sensitive at least to the electrode distance, i.e. the length of the spark, as this quantity will strongly influence the fraction of the spark energy absorbed by the electrodes.

An important practical consequence from the considerations above is that sparks of short duration are energetically more favorable than sparks of long duration, as in the latter case energy is lost

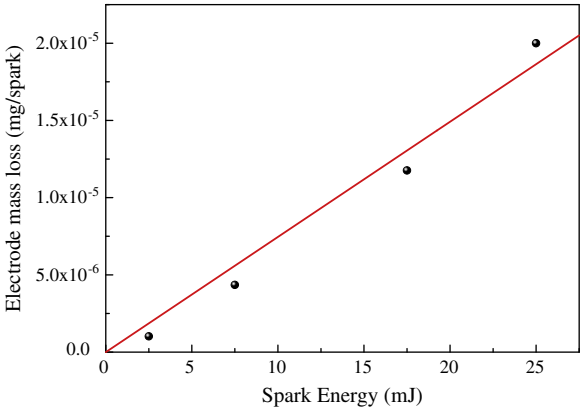

Fig. 4.2. Effect of spark energy on mass production rate ($C = 20$ nF, $d = 1$ mm, $Q = 0.8$ L/min, Ar).

by heat conduction through the electrodes. Indeed, electrode cooling is hardly required in spark generators, and the flowing gas sufficiently does the job. In contrast, continuous arc arrangements can hardly do without electrode cooling.

From the considerations above, the predicted energy required to produce 1 g of gold particles with a 1 mm spark gap is 10^6–10^7 J. Based on the gold data (see Fig. 4.2), a reasonable estimate for the production of a scaled up-spark generator, running at 25 kHz with an E_s of 25 mJ (Section 5), is then 2.25 g h^{-1} for a single electrode pair. Numbering up using parallel electrode pairs can lead to kg quantities, which makes the spark method a feasible technology for industrial production of nanoparticles.

5. Approaches to scaling-up spark nanoparticle generation

The most important industrial applications of spark generated nanoparticles crucially depend upon its scaling potential. The strategy to obtain production rates of industrial magnitude is to proceed in two steps: The mass production rate of a single electrode pair should be maximized, and from there any production rate can be reached by numbering up, i.e. by applying multiple electrode pairs. In the present chapter, we refer to our recent success of increasing the rate of a single electrode pair by two orders of magnitude.

A distinguishing feature of a spark discharge is the high energy, oscillating current pulse that is responsible for electrode ablation. The fast high current pulse is directly responsible for the efficient ablation of material in the spark (Section 4), and the oscillation is useful if one wants to make mixed particles (Section 6). To keep these features during scale-up, we must increase the spark repetition rate, f_{rep}, without modifying the plasma conditions. Spark generators in use today have a limited f_{rep} of ~500 Hz [1], which can be increased to about 1 kHz using expensive capacitor charging supplies fitted with large output resistors.

The typical time until a spark discharge has completely died out is 10 μs, setting the theoretical upper limit of f_{rep} near 100 kHz. When increasing f_{rep} above ~200 Hz with the classical, simple circuit, one inevitably runs into the transition regime to an arc discharge. The breakdown strength of the gas drops due to the residual space charge from preceding sparks, and sparks start forming before the capacitor reaches the desired voltage (Fig. 5.1 vs. Fig. 2.4(b)). Because the energy stored in the capacitance scales with V_c^2, this has a strong impact on particle production.

The problem of early spark formation in the wake of a prior spark can be solved by decoupling the charge and discharge cycles, using a number of switches (Fig. 5.2). By disconnecting the spark gap during the charge cycle, the charge state of the capacitor can be set to an exact value. The spark does not form until switch S_1 is closed, and the capacitor voltage is no longer limited by the breakdown strength of the gas. This allows higher spark energies

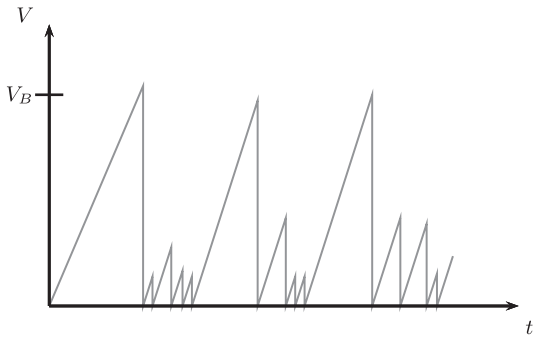

Fig. 5.1. Variations in discharge voltage at higher repetition rates.

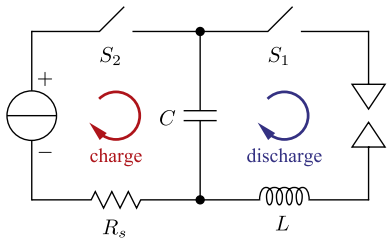

Fig. 5.2. Decoupling charge and discharge cycles.

to be used with low breakdown gases such as He, Ne, and Ar. When closing S_1, a fast ignition must be guaranteed in order to avoid the randomness indicated in Fig. 5.1. To solve this problem, a low-power glow current should be maintained between the pulses, as suggested by the diagram in Fig. 2.4 and further described below.

5.1. Prototype spark forming circuit

The circuit described in Fig. 5.2 requires the use of a high side switch, i.e. logic at high voltage level. Because of the poor availability of suitable switches, we use three 'regular' high voltage switches (1.7 kV, 16 A fast IGBT; IXGR 16N170AH1) in the topology shown in Fig. 5.3. When closing S_1, the left-hand side of the capacitor is forced to 0 V and a negative high voltage pulse hits the top electrode, causing a spark to form. A low-power glow current applied over the gap is necessary to maintain a sufficient space charge to ensure stable spark ignition [18].

Our prototype forms sparks essentially identical to those of the classical circuit (Fig. 5.4 vs. Fig. 2.5(b)). Specifically, the spark duration is short (4 μs), the peak current is high (165 A), and the system oscillates at frequency on the order of 1 MHz. f_{rep} is controlled from 1 to 25 kHz using S_1, rather than being defined by the supplied current. More importantly, the observed waveform of the spark at a given supply voltage stays constant, independent of gas, spark repetition rate or gap spacing. This translates into a constant spark energy of 49.8 (+0.8/−2.4) mJ at 1500 V.

At lower voltages, the spread in applied spark energy increases because the duration of the spark is not controlled. Fig. 5.5 shows two sparks at 1000 V, one lasting two half-cycles, the second three half-cycles of the oscillation. Because of this, the total energy dissipated into the gap varies with ±5%. The obvious solution to this is to quench the spark by opening S_1 after 2 μs. The same approach could be used at higher voltages to reduce spark duration – while keeping the increased peak current.

By keeping the spark energy constant, true scaling up is achieved: Increasing the frequency gives a linear increase in production rate. The results indicate that increasing the quench flow rate proportionally with the frequency yields the expected constant product morphology; a detailed study on this is ongoing by

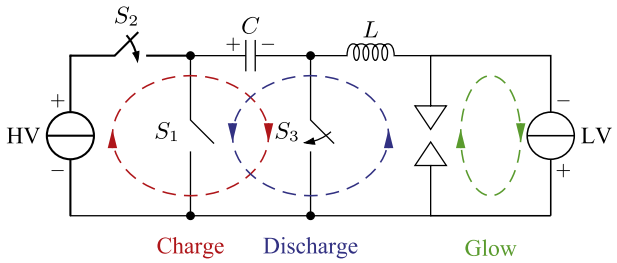

Fig. 5.3. Schematic representation of a pulse forming network, showing current paths for charge and discharge cycles as well as for the continuous glow current. Switches are set to the charging position.

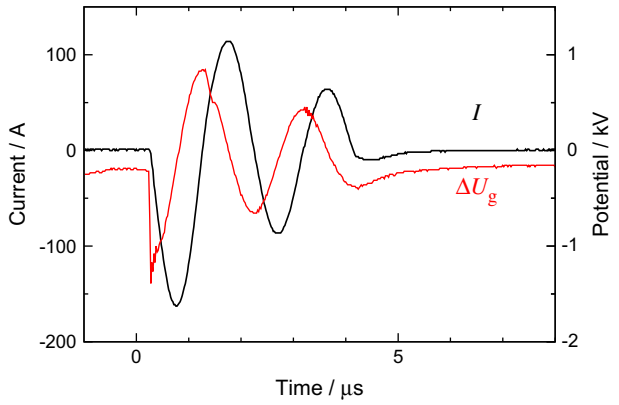

Fig. 5.4. Current and voltage vs. time for the pulse forming network. U supply = 1.5 kV, frep = 1 kHz, quench gas Ar.

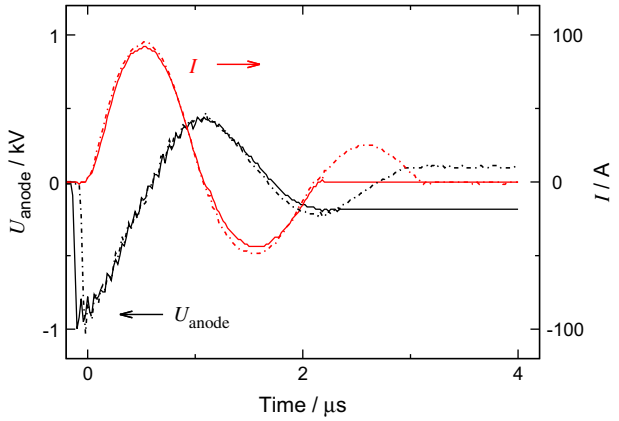

Fig. 5.5. Two oscilloscope traces (dashed and solid) showing variation in spark length. 1.0 kV, 17 kHz, Ar.

Feng et al. With a spark energy of 22.5 mJ, we find for Cu (4 kHz) and Nb (8 kHz) electrode ablation efficiencies of 0.624×10^{-7} and 1.2×10^{-7} g J^{-1} respectively, which is in excellent agreement with prior results of 0.3–1.4 $\times 10^{-7}$ g J^{-1} (Cu) and 0.6–2.5 $\times 10^{-7}$ g J^{-1} (Nb) measured with the classic circuit [25]. With a quench flow of ~130 L/min 99.999% Ar, the collected product consists of oxidized Nb nanoparticles with a primary particle size of 6 nm (σ_g = 1.6).

5.2. Glow discharge

The discharge maintained between the sparks typically is not a stable DC glow, as can be seen from the oscilloscope traces in Fig. 5.6. The average DC current through the gap is ⩽1 mA. Such a current might sustain a weak glow discharge (Fig. 5.6(a)), but is at least three orders of magnitude too low to sustain an arc, and will not result in the ablation of a significant amount of mass from the electrodes [33].

At larger gaps and in argon, the glow is replaced by micro-discharges (Fig. 5.6(b)). The micro-discharges transfer charge from the cathode to the anode, and as a result the cathode voltage and anode voltage (not shown) increase stepwise. The gap voltage ΔU_{gap} remains constant, with dielectric strengths of 8.7×10^5 V m^{-1} for Ar and 1.6×10^5 V m^{-1} for He.

A single micro-discharge is highlighted in Fig. 5.7. The micro-discharges have peak currents in the range of 10–700 mA and appear similar in waveform to the filamentary discharges observed in dielectric barrier discharges [34]. These micro-discharges can re-

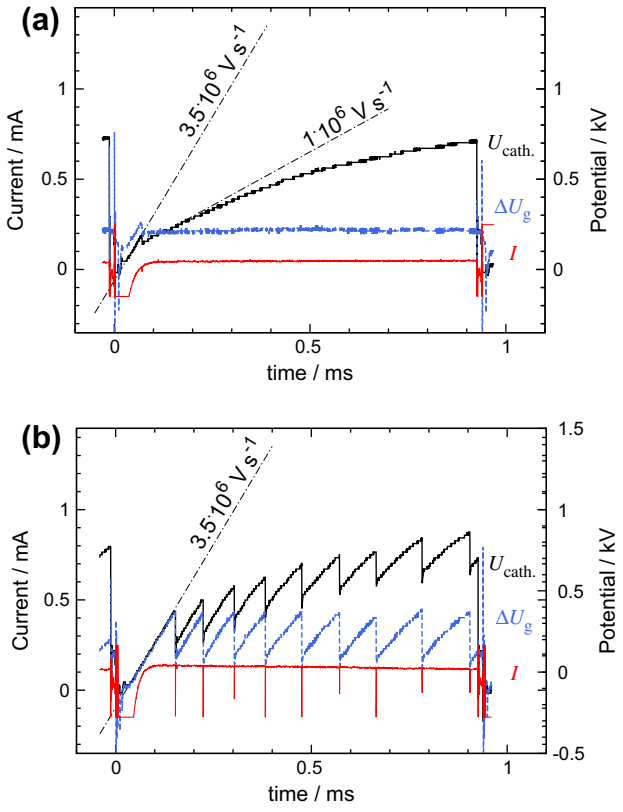

Fig. 5.6. Current and voltage traces of the glow current phase. 0.5 mm gap, US = 1.2 kV and frep = 1 kHz, quench gas 1 L min^{-1}. (a) Glow regime in He, (b) capacitive micro-discharges in Ar.

sult in electrode ablation, and several researchers have worked on particle generators based on DBD [35,36]. The production rates lie many orders of magnitude lower than those of the spark: The only quantitative data available indicates a production rate of 10^{-14} mol s^{-1} for a 9.5 W power input [35], or an ablation efficiency <10^{-14} mol J^{-1}, versus 10^{-9} to 10^{-6} mol J^{-1} for spark discharge. Thus, particle production through micro-discharges can also be neglected.

5.3. Considerations for high frequency sparks

By increasing the repetition rate by two orders of magnitude, the power input increases from tens of W to the kW range. The gas flow rate through the reactor has to be increased to ensure adequate cooling of the electrodes and the gap at the higher power input, keeping a constant dilution over the output power range. As explained in Section 4, the "ideal" spark is short enough to guarantee that all the power transmitted to the electrodes is applied for evaporation, whereas long or continuous discharges result in more power being diverted into electrode heating. This reduces electrode cooling requirements for the spark with respect to the continuous arc, where water cooling is practically inevitable.

The maximum power output of the spark generator circuit is limited by the components used, and the way they are placed and cooled. As an example, C_1 in Fig. 5.3 originally consisted of an array of 20 × 2.2 nF X7R capacitors in parallel that reached thermal limits at 200 W. It was replaced by an array of 96 × 0.47 nF NP0 capacitors in parallel that is rated for >1.25 kW. The limiting components in the prototype circuit are the IGBTs in the charge and discharge paths, which have to conduct short >100 A pulses. IGBT technology is fairly new, and it is reasonable to expect better components, in terms of operating voltage and current, to become available in the near future.

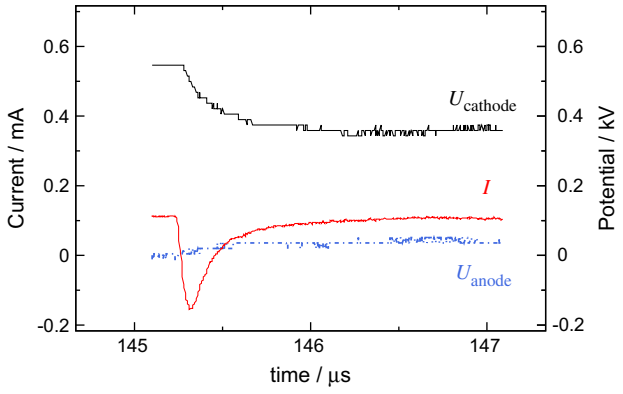

Fig. 5.7. A single micro-discharge, 0.5 mm gap in Ar.

5.4. Conclusion

Nanoparticle production with conventional spark generators is limited by strongly varying spark energies at spark repetition rates above ~500 Hz. By decoupling the charge and discharge cycles of the spark generator, consistent sparks can be obtained at repetition rates on the order of 20 kHz. The sparks of the new spark generator are essentially identical to the oscillating discharges of the conventional circuit, resulting in linear scaling of the production rate.

Space charge is kept in the gap using a superimposed continuous low current, facilitating spark formation. If sufficient current is provided, a glow current can be maintained in small gaps. Otherwise, micro-discharges with energies of 50–100 µJ occur between the electrodes in the dead time between sparks. Both the glow discharge and the micro-discharges are too weak to ablate the electrodes, and can be neglected in terms of nanoparticle production.

The circuit concept introduced has shown to be feasible up to frequencies of 25 kHz. This should produce particle quantities of 2.25 g h^{-1} for gold, as explained in Section 4, and the corresponding order of the production rate is 1 g h^{-1}.

6. Spark mixing, structuring and deposition

6.1. Basic considerations on homogeneous spark mixing

Spark mixing attempts have been published by Byeon et al. [37], and also by Evans et al. [38] but both papers do not show any evidence for mixed phases. The Delft group came out with two studies referring to homogeneous spark mixing of macroscopically miscible and macroscopically immiscible metals in 2009 and 2010 [39,40], respectively. Further studies and applications on spark mixing were subsequently carried out [11,41–43].

The small vapor plume formed by each spark is cooled "instantaneously" by adiabatic expansion and by very rapid mixing with the flowing gas. Slow cooling of the vapor would lead to formation of condensation nuclei, on which further vapor would condense and subsequently the particles formed would grow by collision, according to the classical process of vapor nucleation and condensation. The quenching rate for particle production by continuous arcs is reported to be 10^7 K s^{-1} [44], and much shorter rates, up to 10^{10} K s^{-1} are reported for sparks [16]. Due to the extreme quenching rate and the respective supersaturation in a spark-produced plume, condensation can be modeled by assuming a metal vapor at room temperature, where any atom–atom, atom-particle

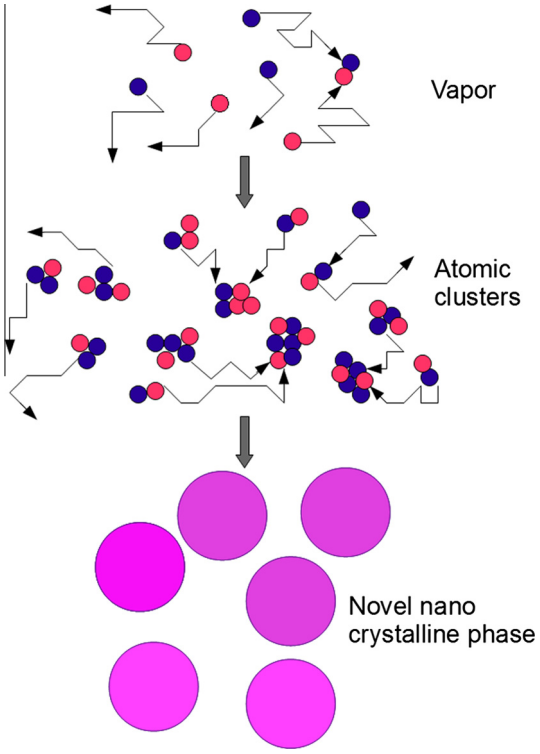

Fig. 6.1. Illustration of particle growth model for spark produced particles: Extreme quenching leads to supersaturation that allows "Smoluchowski growth" from the very beginning, the color of blue and red represents two different materials.

or particle–particle collision leads to sticking. This picture allows application of a Smoluchowski-type coagulation process [45] from the very beginning, as illustrated in Fig. 6.1. At room temperature, sticking can be assumed to occur independent of the material, and most metal particles are solid, not passing through a liquid phase during condensation. The particle formation process must therefore be regarded as quite independent of the melting point or the boiling point of the material. The spark process is also rather independent of the melting point, as pointed out in Section 4 and relatively insensitive to the boiling point, as qualitatively explained below. These two facts explain the excellent mixing capability of the spark process, if atoms of different elements are initially present.

In order to obtain a mixed vapor plume, different concepts have been applied that are illustrated in Fig. 6.2(a)–(c). In the simplest case (a), the electrodes consist of the two different materials A and B to be mixed. Mixed particles are obtained that virtually show all mixing ratios from the pure material A to the pure material B [39,40]. Where alloys of the materials to be mixed exist, alloyed electrodes can be used (Fig. 6.2(b)), and the particle composition corresponds to the composition of the electrodes in the cases studied until now [39]. Where the components to be mixed are not miscible in a wide range of mixing proportions as a macroscopic phase, they may very well be miscible in those proportions within a nanoparticle [40]. Completely new materials can be created this way. Because alloyed rods cannot be formed in this case, a technique has been developed, in which the electrodes are mixed materials on a micron scale (Fig. 6.2(c)), in order to obtain a more uniform distribution of compositions from particle to particle than achievable with different electrodes (Fig. 6.2(a)), [41]. Particles in the micron size range are mixed as a powder and sintered by means of magnetic compaction. This sintering method also bears the potential of adding non-conducting components, as long as the conducting components are present in a high enough concentration to form a continuous phase (percolation) guaranteeing a sufficient conductivity of the electrode.

Because of the potential of creating completely new materials by homogeneous spark mixing with the sintered electrode tech-

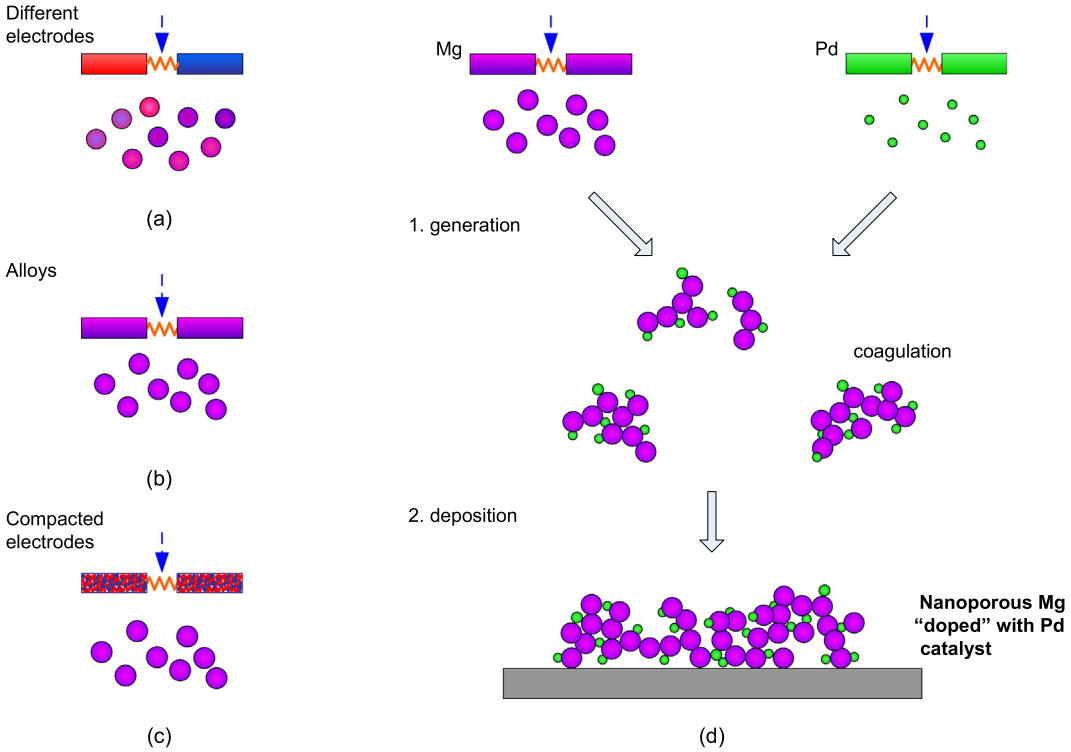

Fig. 6.2. Different principles of spark mixing: atomic mixing (a)–(c) and nanomixing (d).

nique, it is appropriate to add some considerations about the process. Little is presently known, and it is clear that it is a process of high complexity. Some very basic things can be said, though, and these will help in designing future devices for spark mixing. The different substances have different boiling points, and it can be regarded as an amazing experimental result that both are evaporated at about the same rate. This is certainly not the case in normal evaporation or boiling, and we believe that a process referred to as explosive boiling occurs, which is described in a number of publications that refer to laser ablation [27,28], a process that is similar concerning sudden heating of a spot at the surface of a substance. This local sudden heating leads to formation of a superheated liquid layer evolving into a compressed gas, where temperatures and pressures near the critical point, i.e. much higher than the boiling point at normal pressure, can be reached. For example, gold has a boiling point of ~3000 K and a critical point of ~9000 K (@ ~6000 bar). The gas adiabatically expands and forms a shock wave, producing a loud "tick" for each spark. Depending on the conditions, liquid droplets can also be ejected [27], a phenomenon also observed in spark ablation in the form of the round particles in Fig. 3.4. We believe that this superheating phenomenon allows evaporation of both materials with similar rates. To qualitatively understand this phenomenon, it is instructive to take a look at the Hertz–Knutsen equation, expressing the evaporation rate and containing the vapor pressure, which in turn can be expressed by the Clausius–Clapeyron equation [46]. They indicate that the ratio of evaporation rates per unit surface area of two materials of different evaporation enthalpies becomes smaller with increasing temperature. Although the validity of these equations is questionable for the transient process of spark ablation, we do expect that this qualitative statement remains correct. The effect of equal composition of particles and electrodes is effect is observed with alloys [39], even for considerably different boiling points as in the case of Cr–Co. Furthermore, if the evaporation rate per unit surface area of the component with the higher boiling point, and thus also the higher evaporation enthalpy, is still significantly smaller, this component will become enriched at the surface in the initial phase of the spark generator's operation until the evaporation rates correspond to the composition of the electrodes.

Such considerations only give a rough picture. What we learn from them is that the high plasma temperature, feasible only in short sparks, is an important condition for spark mixing on an atomic scale.

6.2. Experimental results on homogeneous spark mixing

Using a pair of different electrodes (Fig. 6.2(a)), the cathode is always ablated most strongly, and switching the anode/cathode materials changes the product composition. The voltage reversal feature explained in Section 2 helps to obtain a more even distribution. Alternatively, voltage reversal can be avoided by introducing a resistor of a few Ohms. It must also be considered that the ablation/evaporation rate is material dependent. Fig. 6.3 shows, how four different average compositions can be obtained by changing the polarity and the circuit resistance [59]. Optimally, a fast switching circuit similar to the one in Section 5 could be used to obtain the desired composition.

Gold and platinum have a large mixing gap in the macroscopic phase diagram. As for a number of other examples, it was shown that spark mixing with the configuration of Fig. 6.2(a) does form a mixed crystalline phase. This is revealed by the XRD spectrum in Fig. 6.4, and the high resolution TEM micrograph in the insert. The colored vertical lines indicate the peak positions for the pure materials, and the broad peaks between them indicate the mixed nanocrystalline phase. The red and blue curves correspond to two different polarities, which slightly modify the mixing ratio.

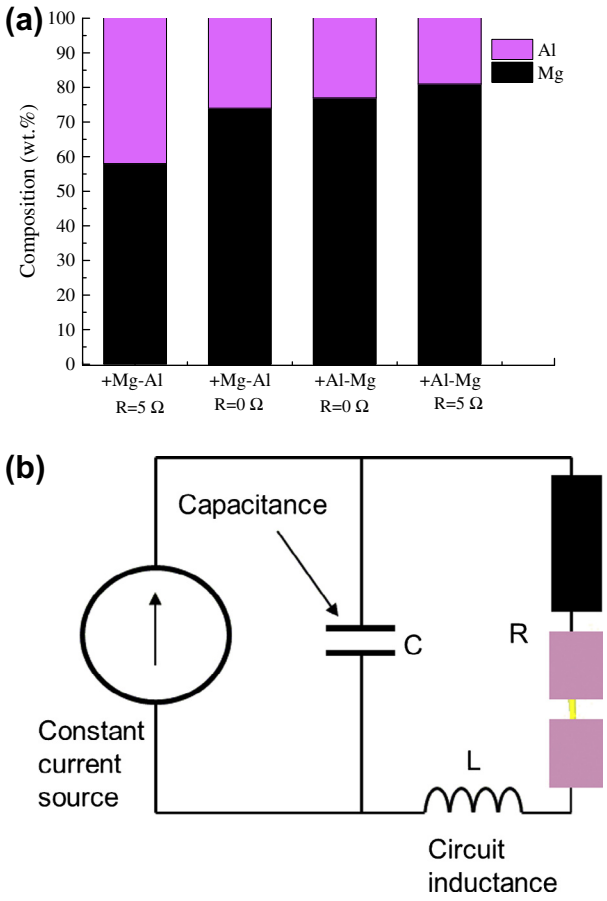

Fig. 6.3. Variation of the average composition of Al–Mg particles produced by the configuration of Fig. 6.2(a), via polarity and damping (with resistance of 0 Ω and 5 Ω) [59].

Traces of large round particles, consisting of a single component, have also formed in this case, as seen in the insert, where a section of the XRD spectrum is strongly amplified (black curve).

Mixing copper and tungsten is impossible in the macroscopic case. In a sintered electrode configuration (Fig. 6.2(c)), Tabrizi et al. [40] produced mixed Cu–W nanoparticles. Evidently, the phases also separate in spark mixing, which is revealed by a series of high-resolution EDS line scans through 6 nm particles in Fig. 6.5. The resolution of the method is about 1 nm, and the compositions strongly vary throughout the particles, showing some sharp slopes. With the resolution in mind, these slopes can be interpreted as sharp boundaries between a copper and a tungsten phase. The scans are consistent with particles consisting of very small domains of pure tungsten and copper, as illustrated in Fig. 6.6. Regarding the resolution, characteristic domain dimensions are probably smaller than 1 nm. The material can thus be considered as composed of atomic clusters, a so-called cluster assembled material [47]. Such materials have very different properties than their crystalline counterparts.

The data in [40] can also be used to obtain some information about the sintered rod mixing concept (Fig. 6.2(c)). This data shows that the mean concentration ratio of Cu and W, determined by XPS, coincides well with the surface composition of the electrodes (39% Cu and 61% W). From a series of 10 randomly chosen primary particle compositions one can calculate a standard deviation, indicating that these values vary, very roughly, by ±15%. Similar variations are observed in various binary systems, mostly independent of whether the electrodes are sintered rods, alloys or pure ele-

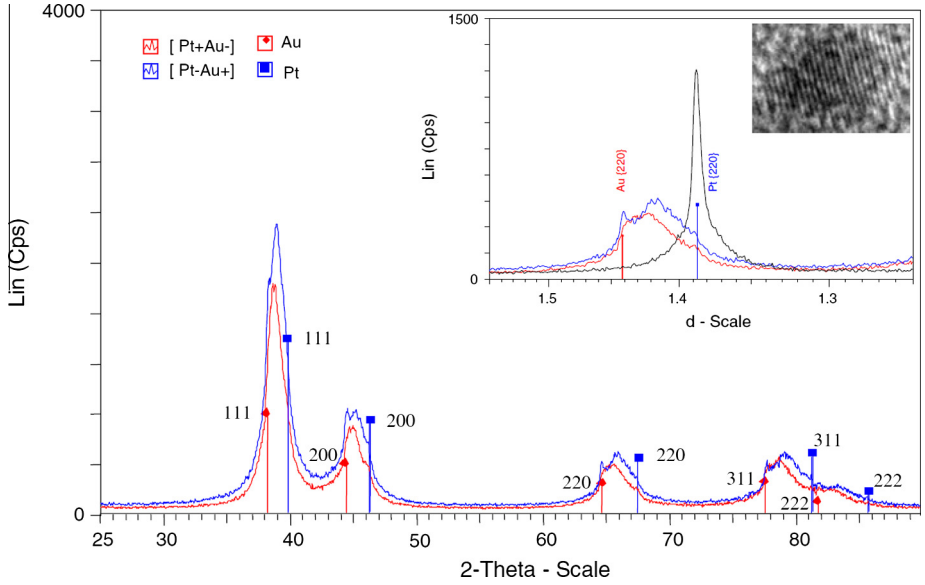

Fig. 6.4. XRD patterns of Au–Pt nanoparticles revealing a mixed nanocrystalline phase. The insert shows a strongly magnified sharp peak due to traces of large particles. The micrograph insert confirms the crystalline mixed phase [40].

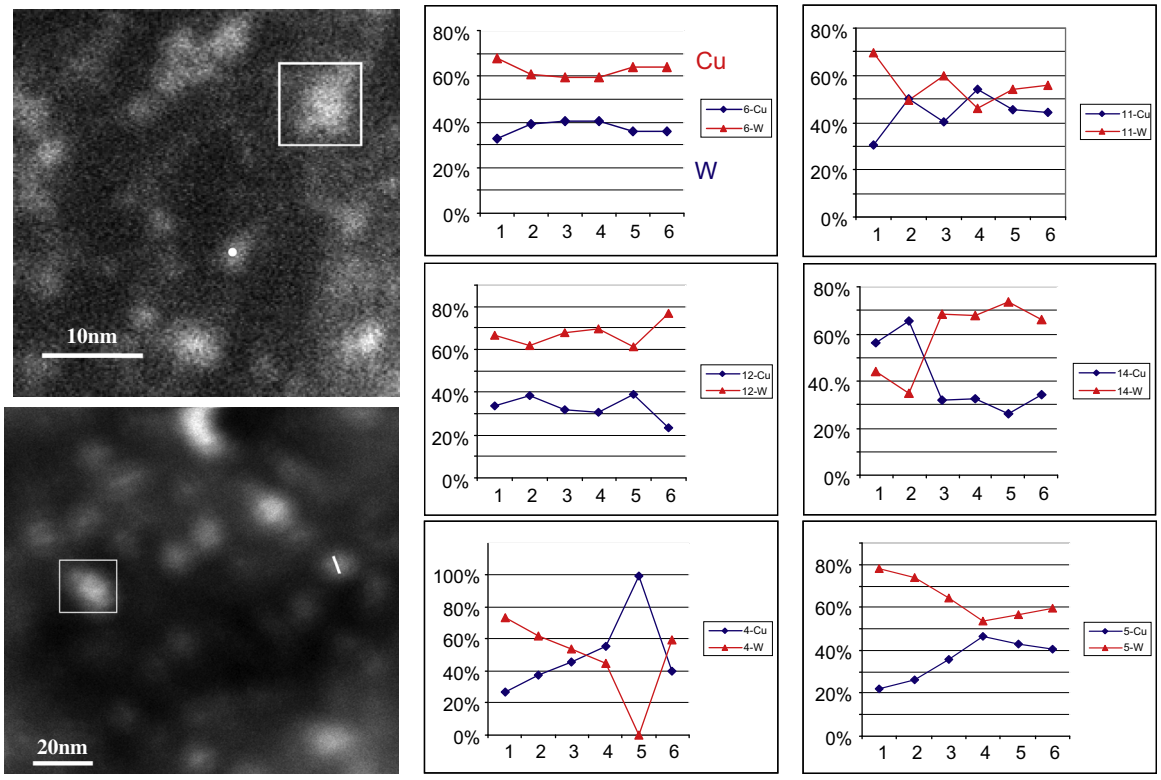

Fig. 6.5. Electron micrographs of Cu–W particles with EDS line scans [40].

ments [39,40]. Particles originating from splashing, well distinguishable through their size and typically consisting of one component only, were excluded in this estimation. There is thus a considerable variation in compositions using the sintered electrodes. This may be improvable by using powders with submicron particles instead of the size of several microns used: Since the diameter of the discharge is also in this size range, as estimated in Section 4, this explains a deviation of the composition from spark to spark.

6.3. Spark nanomixing

In the concept illustrated in Fig. 6.2(d), two spark generated aerosols are mixed very shortly after production. This can be achieved by close proximity of the sparks and turbulent mixing or by putting two spark generator units in series. Such a process leads to co-coagulation of the two components, forming mixed agglomerates, in which the components are mixed on a scale of nanometers. The mixing ratio can conveniently be varied by tuning

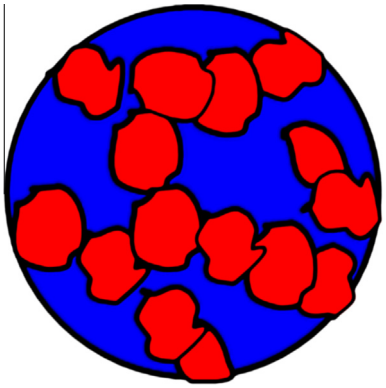

Fig. 6.6. Possible structure in a spark nanomixed Cu–W particle, where the red domains refer to W and the blue ones to Cu or vice versa.

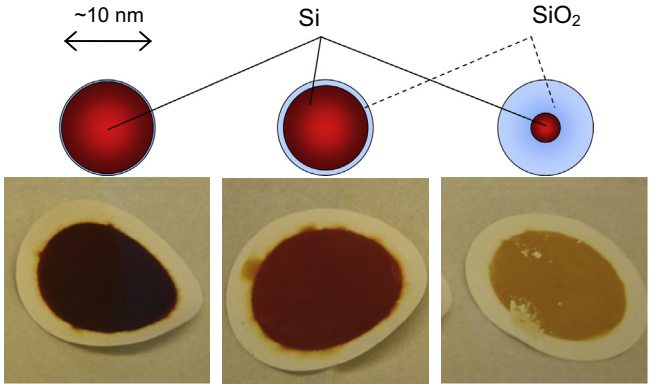

Fig. 6.8. Deposits of Si nanoparticles on filters. The drawing above indicates the stage of oxidation. (Reproduced from Vons et al. [19]).

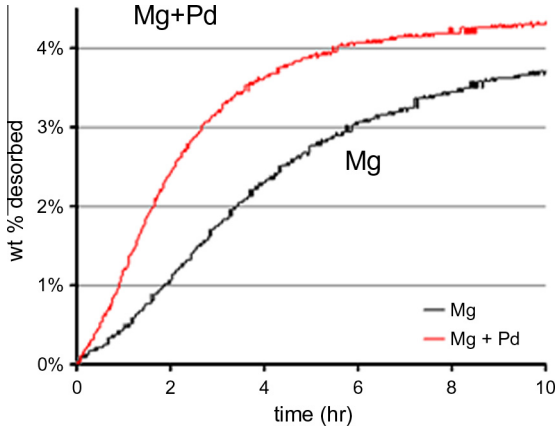

Fig. 6.7. Hydrogen desorption from magnesium hydride with and without addition of small amounts of Pd catalyst by the nanomixing concept of Fig. 6.2(d) [11].

the repetition frequencies. The primary particle diameters of the components can individually be controlled. Magnesium based materials for hydrogen storage have been prepared this way, where magnesium forms a hydride and palladium serves as a catalyst [48] with a mixing ratio of palladium and magnesium of about 1:100. Fig. 6.7 shows the effect of "doping" with a catalyst on hydrogen desorption vs. time, indicating that the material properties regarding this effect have significantly been changed. Mixing Ti into Mg by spark discharge has successfully led to a considerable reduction of the enthalpy for hydride formation, moving this high H-weight percentage hydride closer to application [43].

6.4. Chemical modification of spark produced particles

Being suspended in a gas, the nanoparticles produced can be chemically modified by reacting with gases. Most metals and semiconductors oxidize very easily by mere addition of small amounts of oxygen [11,49]. Aluminum particles have been spark produced to form large agglomerates. By oxidizing after agglomeration, the oxide layer leads to formation of solid bonds between the primary particles and thus rigid agglomerates (aggregates) [50], which have interesting properties for flow visualization. Alternatively, the particles can be collected on a substrate first (see below) to form a rigid porous structure after oxidation, e.g. a matrix for a catalyst. Fig. 6.8 shows deposited spark produced silicon nanoparticles at different stages of oxidation [19]. The color is a convenient indicator for the degree of oxidation.

6.5. Coating of nanoparticles

For passivation of reactive nanoparticles or to modify their properties, particles must often be coated. In the most simple case, a vapor condenses on the particles, while they are in the aerosol. This concept only works if the coating material forms a vapor before the particles to be coated evaporate. A more sophisticated method of coating based on atomic layer deposition (ALD) has been introduced in 2004 [51]. It uses strongly agglomerated "flakes" of nanoparticles in a fluidized bed reactor. The paper shows that the nanoparticles within the agglomerates become individually coated.

A principle of coating nanoparticles in the aerosol state has been introduced by Boies et al. [52]. The aerosol is mixed with a precursor vapor, which is decomposed by UV irradiation. The reaction product forms a homogeneous coating on the particles. Ag nanoparticles were coated with SiO_2 this way.

6.6. Structuring: production of porous materials from spark produced particles

Porous structures form, when nanoparticles or their agglomerates are deposited on surfaces. This can be achieved by filtering, electrostatic precipitation or impaction. With impaction of agglomerated or unagglomerated nanoparticles, porous nanoparticulate layers can be made [53]. The method is suitable for small amounts of material, and chemical sensors can be made this way. As demonstrated earlier, this method works very well with spark produced particles [54]. Fig. 6.9 shows "towers" of nanoparticles that form in an impacting device at a pressure of about 1 mbar. The fibrous structure of these deposits, seen in Fig. 6.9, is remarkable. It indicates that the particles have formed strong bonds in the vertical direction only. This is due to the impact energy, which leads to melting at the contact points. Fig. 6.10 [55] shows a micrograph confirming this, and a model illustration as the insert. By annealing, the lateral contact points can also be sintered, so that a 3-dimensional porous network is formed. For covering larger areas, other deposition methods are more suitable. These concepts allow the combination of arbitrary materials. In principle, a ceramic matrix could be formed, onto which active catalyst particles are nanomixed in the manner described above.

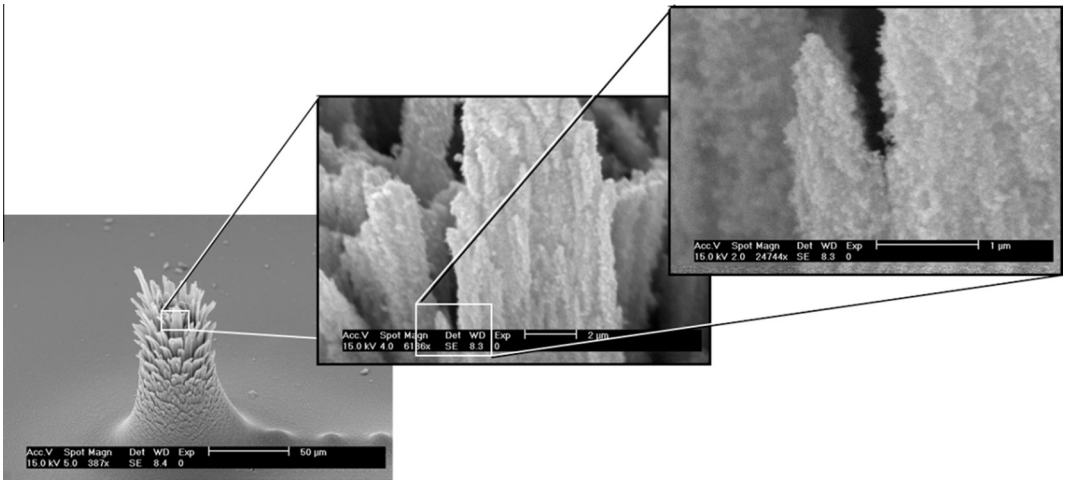

Fig. 6.9. SEM Micrographs of palladium nanoparticles deposited in towers [54].

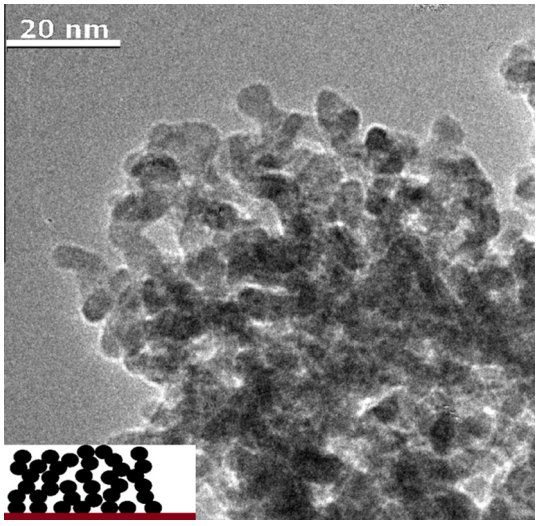

Fig. 6.10. Impacted palladium nanoparticles: TEM micrograph and model (reproduce from Peineke [55]).

7. Conclusion

Production of nanoparticles that are in a size range, where the properties strongly depend on size, are increasingly applied in high-tech materials and devices. The spark discharge method sticks out from other production principles, because it is environmentally friendly, not requiring any solvents or chemical precursors, and not producing any waste. Another important feature in view of application is the achievable particle purity. Being similar to laser ablation, much can be learned from this process to understand spark ablation. The nature of the process is such that it allows simultaneous evaporation of different materials, which co-condense to form new phases that cannot be produced in any other way. This nanomixing feature bears a myriad of possibilities concerning new functional materials, with catalysis as the field that will most obviously benefit. The reason that this has not happened yet is, in our opinion, the absence of concepts for industrial production rates. With the enhancement of the production rate of a single electrode pair to 1 g h^{-1} and the possibility of numbering up, such production rates should now be feasible. The energy requirement should be around 3 kW/g, and can be reduced, e.g. by reducing the spark gap.

Acknowledgements

We gratefully acknowledge the funding from the European Union's Seventh Framework Program under Grant agreement No. 280765 (BUONAPART-E) (J. Feng and A. Schmidt-Ott), as well as from the Dutch funding agency Agentschap.nl under Grant agreement EOS-LT 07052 (T.V. Pfeiffer and A. Schmidt-Ott).

References

[1] B.O. Meuller, M.E. Messing, D.L.J. Engberg, A.M. Jansson, L.I.M. Johansson, S.M. Norlén, N. Tureson, K. Deppert, Review of spark discharge generators for production of nanoparticle aerosols, J. Aerosol Sci. Technol. 46 (2012) 1256–1270.
[2] F. Llewellyn Jones, Electrode erosion by spark discharges, British J. Appl. Phys. 1 (1950) 60–65.
[3] F. Ehrenhaft, PhysikalischeZeitschrift 11 (1910) 619–630.
[4] H. Burtscher, A. Schmidt-Ott, Enormous enhancement of van der Waals forces between small silver particles, Phys. Rev. Lett. 48 (1984) 1734–1737.
[5] S. Schwyn, E. Garwin, A. Schmidt-Ott, Aerosol generation by spark discharge, J. Aerosol Sci. 19 (1988) 639–642.
[6] C. Helsper, W. Molter, Investigation of a new aerosol generator for the production of carbon aggregate particles, Atmos. Environ. 27A (1993) 1271–1275.
[7] A.E. Berkowitz, J.L. Walter, Spark erosion: a method for producing rapidly quenched fine powders, J. Mater. Res. 2 (1987) 277–288.
[8] M. Ullmann, S.K. Friedlander, A. Schmidt-Ott, Nanoparticle formation by laser ablation, J. Nanopart. Res. 4 (2002) 499–509.
[9] J.F. Ready, Development of plume of material vaporized by giant-pulse laser, Appl. Phys. Lett. 3 (1963) 11–13.
[10] M. Kato, Preparation of ultrafine particles of refractory oxides by gas-evaporation method, Jpn. J. Appl. Phys. 15 (1976) 757–760.
[11] V.A. Vons, A. Anastasopol, W.J. Legerstee, F.M. Mulder, S.W.H. Eijt, A. Schmidt-Ott, Low-temperature hydrogen desorption and the structural properties of spark discharge generated Mg nanoparticles, Acta Mater. 59 (2011) 3070–3080.
[12] D. Koch, A.P. Weber, Separation of gas-borne nanoparticles in bubble columns, J. Aerosol Sci. 53 (2012) 61–75.
[13] E.M. Bazelyan, P.R. Yuri, Spark Discharge, 1st ed. CRC-Press, 1998.
[14] J.P. Borra, Nucleation and aerosol processing in atmospheric pressure electrical discharges: powders production, coatings and filtration, J. Phys. D Appl. Phys. 39 (2006) R19–R54.
[15] R. Reinmann, M. Akram, Temporal investigation of a fast spark discharge in chemically inert gases, J. Phys. D Appl. Phys. 30 (1997) 1125–1134.
[16] H. Martinen, H. Tholl. Untersuchung der temperatur und der expansion von funkenkanälen in H_2 bei variabeler energiezufuhr, Zeitschrift für Naturforschung 25a (1970) 430–439.
[17] H. Horvath, M. Gangl, A low-voltage spark generator for production of carbon particles, J. Aerosol Sci. 34 (2003) 1581–1588.
[18] A. Schmidt-Ott, T.V. Pfeiffer, Delft University of Technology, The Netherlands, WO/2013/115644, 2013.
[19] V.A. Vons, L.C.P.M. de Smet, D. Munao, A. Evirgen, E.M. Kelder, A. Schmidt-Ott, Silicon nanoparticles produced by spark discharge, J. Nanopart. Res. 13 (2011) 4867–4879.
[20] W. Koch, S.K. Friedlander, The effect of particle coalescence on the surface area of a coagulating aerosol, J. Colloid Interface Sci. 140 (1990) 419–427.

[21] A.P. Weber, S.K. Friedlander, In situ determination of the activation energy for restructuring of nanometer aerosol agglomerates, J. Aerosol Sci. 28 (1997) 179–192.
[22] A. Schmidt-Ott, In situ measurement of the fractal dimensionality of ultrafine aerosol particles, Appl. Phys. Lett. 52 (1988) 954–956.
[23] S. Kütz, A. Schmidt-Ott, Characterization of agglomerates by condensation induced restructuring, J. Aerosol Sci. 23 (1992) S357–S360.
[24] P. Buffat, J.P. Borel, Size effect on the melting temperature of gold particles, Phys. Rev. A 13 (1976) 2287–2298.
[25] N.S. Tabrizi, M. Ullmann, V.A. Vons, U. Lafont, A. Schmidt-Ott, Generation of nanoparticles by spark discharge, J. Nanopart. Res. 11 (2009) 315–332.
[26] R.A. Petr, T.R. Burkes, Acoustic phenomena in erosion of spark-gap electrodes, Appl. Phys. Lett. 36 (1980) 536–537.
[27] L.V. Zhigilei, Dynamics of the plume formation and parameters of the ejected clusters in short-pulse laser ablation, Appl. Phys. A 76 (2003) 339–350.
[28] A. Miotello, R. Kelly, Laser-induced phase explosion: new physical problems when a condensed phase approaches the thermodynamic critical temperature, Appl. Phys. A 69 (1999) 67–73.
[29] F.E. Kruis, H. Fissan, B. Rellinghaus, Sintering and evaporation characteristics of gas-phase synthesis of size-selected PbS nanoparticles, Mater. Sci. Eng. B69–70 (2000) 329–334.
[30] E. Hontañon, F.E. Kruis, A Differential Mobility Analyzer (DMA) for size selection of nanoparticles at high flow rates, Aerosol Sci. Technol. 43 (2009) 25–37.
[31] A. Hussin, H.G. Scheibel, K.H. Becker, J. Porstendörfer, Bipolar diffusion charging of aerosol particles–I: experimental results within the diameter range 4–30 Nm", J. Aerosol Sci. 14 (1983) 671–677.
[32] P. Milani, M. Ferretti, P. Piser, C.E. Bottani, A. Ferrari, A. Li Bassi, G.. Guizzetti, M. Patrini, Synthesis and characterization of cluster-assembled carbon thin films, J. Appl. Phys. 82 (1997) 5793–5798.
[33] A. Fridman, Plasma Chemistry, 1st ed., Cambridge University Press, New York, 2008.
[34] N. Jidenko, M. Petit, J.-P. Borra, Electrical characterization of microdischarges produced by dielectric barrier discharge in dry air at atmospheric pressure, J. Phys. D Appl. Phys. 39 (2006) 281–293.
[35] J. Hou, N. Jidenko, J.-P. Borra, A.P. Weber, Production of metal nanoparticles in asymmetrical dielectric barrier discharge-plasma reactor at atmospheric pressure, ChemieIngenieurTechnik 83 (2011) 2161–2169.
[36] E. Bourgeois, N. Jidenko, J.-P. Borra, Nano-particles Production by Dielectric Barrier Discharge. Paper presented during the International Aerosol Conference, 2010, Helsinki, Finland.
[37] J.H. Byeon, J.H. Park, J. Hwang, Spark generation of monometallic and bimetallic aerosol nanoparticles, J. Aerosol Sci. 39 (2008) 888–896.
[38] D.E. Evans, R.M. Harrison, J.G. Ayres, The generation and characterization of metallic and mixed element aerosols for human challenge studies, Aerosol Sci. Technol. 37 (2003) 975–987.
[39] N.S. Tabrizi, Q. Xu, N.M. van der Pers, U. Lafont, A. Schmidt-Ott, Synthesis of mixed metallic nanoparticles by spark discharge, J. Nanopart. Res. 11 (2009) 1209–1218.
[40] N.S. Tabrizi, Q. Xu, N.M. van der Pers, A. Schmidt-Ott, Generation of mixed metallic nanoparticles from immiscible metals by spark discharge, J. Nanopart. Res. 12 (2010) 247–259.
[41] U. Lafont, L. Simonin, N.S. Tabrizi, A. Schmidt-Ott, E.M. Kelder, Synthesis of nanoparticles of Cu, Sb, Sn, SnSb and Cu_2Sb by densification and atomization process, J. Nanosci. Nanotechnol. 9 (2009) 2546–2552.
[42] A. Anastasopol, T.V. Pfeiffer, A. Schmidt-Ott, F.M. Mulder, S.W.H. Eijt, Fractal disperse hydrogen sorption kinetics in spark discharge generated Mg/NbO_x and Mg/Pd nanocomposites, Appl. Phys. Lett. 99 (2011). 194103-194103-3.
[43] A. Anastasopol, T.V. Pfeiffer, J. Middelkoop, U. Lafont, R.J. Canales-Perez, A. Schmidt-Ott, F.M. Mulder, S.W.H. Eijt, Reduced enthalpy of metal hydride formation for Mg–Ti nanocomposites produced by spark discharge generation, 135 (2013) 7891–7900.
[44] N.T. Jenkins, T.W. Eager, Submicron particle chemistry: vapor condensation analogous to liquid solidification, JOM 55 (2003) 44–47.
[45] M. von Smoluchowski, Mathematical theory of the kinetics of the coagulation of colloidal solutions, Z. Phys. Chem. 92 (1917) 129–168.
[46] C. Peineke, M. Attoui, A. Schmidt-Ott, Using a glowing wire generator for the production of charged, uniformly sized nanoparticles at high concentrations, J. Aerosol Sci. 37 (2006) 1651–1661.
[47] K. Sattler, Cluster Assembled Materials (Materials Science Forum), 1st ed., Trans Tech Publications, Switzerland, 1996.
[48] V.A. Vons, H. Leegwater, W.J. Legerstee, S.W.H. Eijt, A. Schmidt-Ott, Hydrogen storage properties of spark generated palladium nanoparticles, Int. J. Hydrogen Energy 35 (2010) 5479–5489.
[49] C. Roth, G.A. Ferron, E. Karg, B. Lentner, G. Schumann, S. Takenaka, J. Heyder, Generation of ultrafine particles by spark discharging, Aerosol Sci. Technol. 38 (2004) 228–235.
[50] S. Ghaemi, A Schmidt-Ott, F. Scarano, Nanostructured tracers for laser-based diagnostics in high-speed flows, Meas. Sci. Technol. 21 (2010) 105403 (10pp).
[51] R.J. Wank, S.M. George, A.W. Weimer, Nanocoating individual cohesive boron nitride particles in a fluidized bed by ALD, Powder Technol. 142 (2004) 59–69.
[52] A.M. Boies, J.T. Roberts, S.L. Girshick, B. Zhang, T. Nakamura, A. Mochizuki, SiO_2 coating of silver nanoparticles by photoinduced chemical vapor deposition, Nanotechnology 20 (2009) 295604 (8pp).
[53] I. Aruna, F.E. Kruis, S. Kundu, M. Muhler, R. Theissmann, M. Spasova, CO ppb sensors based on monodispersed SnOx: Pd mixed nanoparticle layers: insight into dual conductance response, J. Appl. Phys. 105 (2009). 064312-064312-8.
[54] C. Peineke, A. Schmidt-Ott, Atomic Clusters produced by a Glowing Wire, Proc, PARTEC, 2007.
[55] C. Peineke, Production and Deposition of Well Defined Aerosol Nanoparticles for Studies on Basic Properties, PhD thesis, Delft University of Technology, Delft, 2008.
[56] S. Kala, M. Rouenhoff, R. Theissmann, F. Einar Kruis, Synthesis and Film Formation of Monodisperse Nanoparticles and Nanoparticle Pairs. In: Nanoparticles from the Gasphase: Formation, Structure, Properties, Axel Lorke, Markus Winterer, Roland Schmechel, and Christof Schulz [Ed.], NanoScience and Technology. Springer, (2012) 99–119.
[57] J.H. Byeon, J.-W. Kim, Production of carbonaceous nanostructures from a silver–carbon ambient spark, Appl. Phys. Lett. 96 (2010) 153102.
[58] H. Förster, W. Peukert, In-Situ Synthesis and Functionalisation of Metal Nanoparticles in a Spark Discharge Process, presented at the International Aerosol Conference 2010, Helsinki, Finland (2010), 1234.
[59] V.A. Vons, Spark Discharge Generated Nanoparticles for Hydrogen Storage Applications. Dissertation, Delft University of Technology, 2010, p. 164.